https://dx.doi.org/10.1016/j.cej.2024.149006

Thermally Managed and Fireproof Composite Aerogels for Safer and Year-Round Energy Saving

Wei Cai [a,b,1], Zhaoxin Li [a,1], Heng Xie [c], Wei Wang [d], Tianyang Cui [a], Bicheng Lin [a], Liangyuan Qi [a], Xin Hu [b], Yu Du [c], Yang Ming [b], Shuo Shi [b], Daming Chen [b], Bin Fei [b], Weiyi Xing [a*], Yuan Hu [a]*

[a]State Key Laboratory of Fire Science, University of Science and Technology of China, Hefei 230026, PR China

[b]School of Fashion and Textiles, The Hong Kong Polytechnic University, 999077, Hong Kong S.A.R, China

[c]School of Chemistry and Chemical Engineering, Huazhong University of Science and Technology, Wuhan, 430074, PR China

[d]School of Mechanical and Manufacturing Engineering, University of New South Wales, Sydney, NSW 2052, Australia

* Corresponding author

E-mail: xingwy@ustc.edu.cn (W. Xing); bin.fei@polyu.edu.hk (B. Fei)

[1]These authors contributed equally to this work.

Abstract: Seasonable and spontaneous replacement approach of daytime radiative cooling to solar thermal conversion is challenging yet imperative for year-round thermal management materials. Meanwhile, the fire safety of thermal management materials is extremely important but often overlooked. Herein, we report a bio-inspired and fireproof aerogel presenting dynamically self-switchable ability of daytime radiative cooling and solar thermal conversion, composed of thermochromic microcapsules (TC), boron nitride nanosheets (BN), and bio-based materials (alginate and phytate). In hot environments, TC/BN composite aerogel shows solar reflectivity of 91.8% and IR emissivity of 84.3%, promoting heat radiation to outer space and achieving an average temperature drop of ~5.62 °C. Attributed to the thermochromic

mechanism, TC/BN composite aerogel can harvest visible light of 87% in the solar spectrum to increase the material temperature by 28.3 °C, under an environment of -8.8 °C. Based on the EnergyPlus simulation, the employment of TC/BN composite aerogel contributes to decreasing the energy consumption of buildings in both hot and cold regions, including Cairo, Singapore, Alaska, Yakutsk, and so on. Besides, the peak values of heat release rate and total heat release during the combustion of TC/BN composite aerogels are significantly decreased by 70.6% and 58.4%, compared to those of TC composite aerogel. The produced protective char layer enhanced by BN nanosheets is capable of isolating the fire and suppressing the fire propagation, improving the fire safety of composite aerogels designed. The TC/BN composite aerogels provide a smart thermal regulation mode for radiative cooling and solar heating, overcome the problems from changing weather and environment, and significantly promote the practical application by enhanced fire safety.

Keywords: Fireproof performance; bio-based aerogels; Solar reflection and radiative cooling; Solar absorption and conversion

1. Introduction

Carbon neutrality by 2050 is undoubtedly the world's most imperative mission with the growth of global climate change and energy crisis. The building sector accounts for approximately 31% of global final energy consumption and more than 30% of the entire worldwide CO_2 emission[1]. The significant energy consumption in buildings is mainly attributed to the indoor temperature control system, i.e., heating and cooling. It is a huge challenge to develop an energy-saving and sustainable technology to regulate the room temperature, replacing the traditional air-conditioning technique. Recently, solar heating and radiative cooling effects, which can convert solar energy into heat or radiate heat energy through atmospheric window, have been regarded as two advanced and effective approaches to change the indoor temperature[2-4]. For example,

photo-thermal materials coated onto the building surface can absorb solar energy and deliver effective heat to indoor. Besides, passive cooling materials are able to reflect solar energy and radiate heat through atmospheric window[5-9]. Therefore, it is believed that the integration and seasonal employment of solar heating and radiative cooling effects can effectively decrease energy consumption in buildings. In an ideal condition, the solar reflectance in hot summer should be close to 100%, thus avoiding the unfavorable effects of overmuch solar energy (**Figure** 1a). Different from hot summer, the ideal solar absorbance in cold winter should be increased as far as possible (**Figure** 1b). However, solar heating and radiative cooling are related tightly to solar absorption and reflection, respectively[10]. Due to the opposite mechanism in solar absorption and reflection, integrating the effects of solar heating and radiative cooling onto the building surface is a huge challenge and extra energy sources, such as electricity and mechanical energy, are required usually for material replacement seasonally[11, 12]. Besides, the application fields of thermally managed materials focus on the surface of buildings and human skin, tightly relating to fire safety problems. In particular, the polymer-based thermally managed materials are flammable and easily ignited to release a mass of heat and toxic gas, causing loss of life and personal injury. However, the fire hazards of thermally managed materials are usually ignored.

There is an interesting phenomenon that some birds and animals, such as ptarmigan and polar hare, will change their hair color according to the seasonal change (**Figure** 1c). It is attributed to the adjustment mechanism of melatonin, reported by the previous literature[13]. Inspired by the seasonal color molting in mammals, fortunately, the development of thermochromic materials provides a new and adjustive ability to photo-thermal conversion and passive radiative cooling, facing different seasons and temperatures[14, 15]. As one kind of thermochromic materials, temperature-responsive melanin is composed of fluorane, bisphenol A, and aliphatic alcohol. At different temperatures, aliphatic alcohol will be in a molten state or solidification state. Fluorane is not dissolved into aliphatic alcohol in any state, while bisphenol A can be

dissolved into molten aliphatic alcohol. Therefore, in a warm environment, bisphenol A and fluorane will be separated. On the contrary, in a cold environment, bisphenol A and fluorane will be blended and form a conjugated structure to absorb and convert solar energy, with the generalized acid-base neutralization reaction between phenolic hydroxyl and amino groups (**Figure** 1d). It is believable that, based on the adjustive effect, thermochromic materials are capable of harvesting solar energy in cold winter and reflecting solar energy in hot summer, presenting a smart thermal regulation function. Meanwhile, once the radiative cooling effect is introduced, the smart thermal regulation effect of thermochromic materials will be significantly promoted.

Herein, inspired by the seasonal color molting in birds and animals, a smart composite aerogel towards seasonal thermal regulation is developed by integrating thermochromic microcapsules, boron nitride nanosheets, and bio-based alginate and phytate. Due to the multiple reflections in the air-aerogel interfaces, the solar reflection of composite aerogel is up to 91.8%. Along with high IR emissivity, TC/BN composite aerogel presents an effective radiative cooling effect. Attributed to the temperature-responsive melt characteristic of aliphatic alcohol, TC/BN composite aerogel can present an obvious photo-thermal conversion effect. As confirmed by the EnergyPlus simulation, as-prepared TC/BN composite aerogel can decrease the energy consumption of buildings located in both hot (i.e., Cairo, Singapore, and New Delhi) and cold (i.e., Alaska, Mohe, and Yakutsk) cities. Meanwhile, the fireproof performances are also presented by TC/BN composite aerogel, enhancing the application safety.

2. Materials and methods

2.1. Raw materials

Bisphenol A (AR), melamine (AR), and 37% formaldehyde solution (AR) were provided by Aladdin Industrial Co., Ltd. (Shanghai, China). 2-Anilino-6-dibutylamino-3-methylfluoran (AR), n-decanol (AR), lauryl alcohol (AR), sodium alginate (AR), sodium phytic (AR), and

sodium dodecyl sulfonate (AR) were purchased from Sinopharm Chemical Reagent Co., Ltd. Hexagonal boron nitride (h-BN, AR) with a purity of 98.5% was purchased from Aladdin Industrial Co., Ltd. (China), of which the average particle size was about 1 μm.

2.2. The preparation of thermochromic microcapsules

Based on this classical microencapsulation technology, the thermochromic microcapsule was prepared using melamine resin as shell material. Firstly, bisphenol A, 2-Anilino-6-dibutylamino-3-methylfluoran, and aliphatic alcohol were added into an aqueous solution, with a mass ratio of 1:2:97. Meanwhile, the aliphatic alcohol is a mixture of n-decanol and lauryl alcohol with a mass ratio of 56:44. Employing sodium dodecyl sulfonate as a surfactant, a steady O/W emulsion was formed with a mechanical stirring (3000 r/min) for 60 min. Melamine and 37% formaldehyde solution were mixed and reacted with a pH value of 8.5, forming the pre-polymer of melamine resin which was slowly added to the above emulsion dropwise. During the microencapsulation process, the pH value of this reaction system was adjusted to 4. After the microencapsulation process of 6h, the synthesized product, i.e., thermochromic microcapsule, was collected by vacuum filtration.

2.3. The preparation of TC/BN composite aerogels

The unidirectional freezing method was employed to prepare bio-inspired composite aerogels. BN nanosheets were prepared according to previous literature[16]. Based on the function of individual modules, 1.0g BN nanosheets, 1.0g sodium alginate (SA), 0.3g sodium phytate, and 0.5g TC microcapsule were added to an aqueous solution of 200 mL. The mixed solution was stirred for 1h with sonication, thus obtaining well-dispersed BN nanosheets and TC microcapsule. A slant copper platform was first put into liquid nitrogen to obtain an extremely temperature. Then, the precursor solution of composite aerogel contained by polytetrafluoroethylene mold was put onto the surface of the slant copper platform for 30 min, thus achieving a unidirectional freezing structure. The completely frozen solution was freeze-dried to prepare bio-inspired TC/BN composite aerogel.

2.4. Characterization

The structure and features of composite aerogel were observed with an XL-30 ESEM scanning electron microscope (SEM) at an acceleration voltage of 20.0 kV. Transmission electron microscopy (TEM) was used to observe BN nanosheets with a JEOL JEM-2100F transmission electron microscope at an accelerating voltage of 200 kV. The contact angle was determined by an SL200B Contact Angle System (Solon Tech. Co., Ltd., China) at ambient temperature. At least five points were detected for each sample. Thermogravimetric analysis (TGA) was executed with a TGA Q5000 IR thermogravimetric analyzer (TA Instruments, U.S.) at a heating rate of 20 ^{o}C min^{-1}. A combustion test was performed on a cone calorimeter (Fire Testing Technology, UK) according to ISO 5660 standard procedures, with 100 × 100 × 5 mm^3 specimens. Each specimen was exposed horizontally to 35 kW/m^2 external heat flux. All samples were tested three times. Thermogravimetric analysis-infrared spectrometry (TG-IR) was investigated with a TGA Q5000IR thermogravimetric analyzer linked to a Nicolet 6700 FTIR spectrophotometer from 20 to 700 ^{o}C at 10 ^{o}C /min (N_2 atmosphere, flow rate of 30 mL/min). The micro-sized combustion behavior of TC and TC/BN composite aerogels was performed on a microscale combustion calorimeter. Differential scanning calorimetry (DSC) was conducted using a Q25 instrument (TA, USA) at a heating rate of 5 K/min from -20 to 50 °C under a nitrogen atmosphere. The light intensity of the Xe lamp and solar are measured by a light intensity meter (TES-1333). The mechanical performance of TC/BN composite aerogel is studied by the compression test, by a universal testing machine with a digital force gauge (DS2, ZHIQU Precision Instruments) of a 100 N load at a displacement rate of 10 mm/min at 50% compression strain. N_2 adsorption-desorption isotherms were performed at 77 K using 3H-2000PS1 specific surface and pore size analysis instrument (BeiShiDe Instruments, China). The specific surface area was calculated according to the Brunauer-Emmett-Teller (BET) method.

2.5. Radiative cooling and Photo-thermal conversion test

UV-vis-NIR spectroscopy was performed using a Perkin-Elmer LAMBDA 1050 high-performance UV-vis-NIR double-beam spectrophotometer. The emittance spectra were obtained by measuring reflectance (R) and transmittance (T), which were calculated as 1-R-T. According to Kirchhoff's law, emittance is equivalent to absorptance when an object is in thermodynamic equilibrium. Outdoor cooling performance was measured using a self-assembled radiant refrigeration performance test device in Hefei, China. A homemade measurement system mainly consisting of cold hydrazine with a diameter of 35.0 cm and a height of 50.0 cm, a Xe lamp (CELPE300L-3A), an IR camera (FLIR-E95), and a digital camera (FDRAX700 4K) was used to investigate the photo-thermal conversion effect under cold enviroment. After being radiated by simulated solar light of 1.0 kW/m^2, the surface temperature and appearance of TC/BN composite aerogel were recorded to evaluate the photo-thermal conversion performance. The humidity ranged from 70% to 80% and the test pressure is 101.325 kPa, i.e., standard atmospheric pressure.

2.6. EnergyPlus simulation

The length, width and height of each floor of building model are 40m, 20m, and 4m. The layer number of building model is 8. Meanwhile, the height of glass is 1.5m. The TC/BN composite aerogel cover onto the surface of building model, excluding rooftop and glass. The thickness of TC/BN composite aerogel layer is 3.0 mm. The thermal conductivity, density, specific heat capacity, and IR emissivity of TC/BN composite aerogel set as 0.04 W/mK, 0.0175 g/cm^3, 1.5 kJ/(kg*K), and 0.843. The control sample is $CaCO_3$. With same thickness, The thermal conductivity, density, specific heat capacity, and IR emissivity of $CaCO_3$ set as 0.05 W/mK, 0.0175 g/cm^3, 1.5 kJ/(kg*K), and 0.700. The solar and visible absorptivity of $CaCO_3$ are 0.1 and 0.1. In cold cities, the solar and visible absorptivity of TC/BN composite aerogel are 0.545 and 0.870. In hot cities, the solar and visible absorptivity of TC/BN composite aerogel are 0.082 and 0.098. Cairo, Singapore, and New Delhi are chosen as hot cities and Alaska, Mohe, and

Yakutsk are chosen as cold cities. The ideal air condition system is used in this simulation, without the energy limiting. The heating and cooling critical temperature is 20 ºC and 26 ºC.

3. Results and Discussion

3.1. Production of bio-inspired composite aerogels

Inspired by the molting phenomenon of animals and birds, a smart and thermochromic material is developed with the classical microencapsulation technology (**Figure** 1e). Firstly, pre-polymer of melamine resin was used for the encapsulation of bisphenol A, 2-Anilino-6-dibutylamino-3-methylfluoran, and aliphatic alcohol, thus preparing thermochromic microcapsules. Secondly, a directional-freezing method was employed to prepare bio-based composite aerogels (**Figure** 1f). The significant temperature gradient promoted the directional growth of the aerogel structure[17, 18]. With the addition of TC microcapsules, the prepared composite aerogel not only converts solar energy to heat in cold weather, but also reflects the solar energy and delivers heat to outer space in hot weather (**Figure** 1g).

As presented in **Figure** S1, the synthesized thermochromic microcapsules demonstrate an appearance of gray-white. This phenomenon indicates that a small number of bisphenol A and 2-anilino-6-dibutylamino-3-methylfluoran is reacted, may attributed to the slight solidification of mixed fatty alcohol at low temperature (~14 ºC). Removed from an environment temperature of 0 ºC, thermochromic microcapsule gradually transition to gray-white from black, within 180s, corresponding to the gradual melting process of mixed fatty alcohol (**Figures** 2a and S2). The micro-morphology of thermochromic microcapsules is studied by SEM photographs, presenting a typical spherical structure (**Figures** 2b_1 and S3). Obviously, the scale of the most thermochromic microcapsules is from 2 μm to 5 μm and has a uniform grain diameter dispersion (**Figure** 2b_1). The phase change temperature of thermochromic microcapsules is determined by the DSC curve (**Figure** 2b_2). The endothermic peaks related to the melting process of fatty alcohol are between 4.9 and 13.7 °C. This temperature range is also corresponding to the color

change of white to black of thermochromic microcapsules. In addition, the long-term performance of TC microcapsules during the solid/molten cycles is studied by a multi-cycle DSC scan (**Figure** S4). Even with cycle tests of up to 50 times, all the endothermic curves were similar to the initial curve, showing that the TC microcapsules have excellent phase transition stability[19]. With the sonication process in a liquid phase, bulk BN powder was successfully exfoliated into a sheet structure, with 500 nm in length (**Figure** S5). The digital photo and 3D schematic of the prepared TC/BN composite aerogel are presented in **Figures** $2c_1$ and $2c_2$. During the formation of ice crystals, BN, SA, PA, and TC microcapsules will be repelled from the suspension solution. Meanwhile, due to the directional heat loss caused by the copper platform, the large temperature gradient promoted the vertical growth of ice crystals. The top surface presents a disorder morphology, while the parallel skeleton structure in cross-section indicates a directional growth mechanism (**Figures** $2d_1$ and $2d_2$). A large number of voids with ultrathin cell walls implies a low density (**Figure** $2d_3$). In addition, some TC microcapsules are covered on the walls (**Figure** $2d_4$). The chemical elements of TC/BN composite aerogel are determined by SEM-EDS Mapping (**Figure** $2d_5$). The element signals of B, N, O, and C elements are consistent with the major materials, i.e., sodium alginate and boron nitride. The ordered element distribution also confirms the directional structure of TC/BN composite aerogel. The specific surface area of composite aerogel was calculated by the Brunauer-Emmett-Teller (BET) method, which is up to 9.986 m^2/g (Figure S6). Combined with the soft and rigid nature of SA and BN nanosheets, this as-prepared composite aerogel exhibited high strength to compression (Figure S7). At 0 ^oC, the compression strength of TC/BN composite aerogel is up to 0.380 MPa. With a higher test temperature (30 ^oC), the fatty alcohol melts and slightly decreases the corresponding compression strength to 0.323 MPa. Even though the fatty alcohol will be melted into liquid at a relatively high temperature, the shell material prepared by melamine resin still maintains the solid state to package the melted fatty alcohol. Therefore, the mechanical properties of TC/BN aerogel composites are not influenced obviously by this

melt behavior. Under simulated sunlight of 1.0 kW/m^2, the surface temperature of TC/BN composite aerogel is gradually increased to ~49.8 ^{o}C from 32.1 ^{o}C, achieving an equilibrium temperature of ~49 ^{o}C in 100s (**Figure** 2e, S8, and S9). Compared to TC/BN composite aerogel, TC composite aerogel without BN nanosheets presents a slightly higher equilibrium temperature, near 53.1 ^{o}C at 150 s (bottom right corner in **Figure** 2e). The IR thermal images corresponding to the time of TC/BN composite aerogel are presented in **Figure** S8. Given the environment temperature of ~30 ^{o}C, the temperature increase of only ~19.8 ^{o}C in TC/BN composite aerogel is relatively weak and attributed to the reflection effect of BN nanosheets and porous structure in aerogel[20-22]. Meanwhile, the equilibrium temperature of low to ~49 ^{o}C also confirms its potential in the radiative cooling performance (Figure S9).

3.2. Thermal regulation performance of bio-inspired composite aerogels

Based on the UV-vis-near IR spectrum, the solar absorption of BN nanosheets, SA, and TC microcapsules under room temperature are investigated (**Figure** 3a$_1$). It is found that both SA and TC microcapsules present a high absorption capability to UV (300-380) and visible light (380-760 nm). Ranging from 250 nm to 640 nm of solar wavelength, solar absorption of both TC and SA is more than 27.8%. Due to the large bandgap and high refractive index, an obvious solar reflection is presented onto the surface of BN nanosheets, thus obtaining solar absorptivity of ~20% in the whole solar waveband. Therefore, the introduction of BN nanosheets is able to improve the solar reflection of composite aerogels at normal temperatures, avoiding the unfavorable effect caused by solar energy. As expected, the addition of BN nanosheets significantly decreases the solar absorption of TC/BN composite aerogel (**Figure** 3a$_2$). For example, from 400 nm to 600 nm, solar absorption of TC composite aerogel is near 40%. With the high reflectivity of BN nanosheets, the solar absorption of TC/BN composite aerogel in the same waveband is decreased to 20%[23]. To compare the solar absorptions of TC and TC/BN

composite aerogels more clearly, the solar absorption in the whole wavelength was calculated according to the following equation[24]:

$$\alpha(\lambda,\theta,\varphi) = \int_{\lambda min}^{\lambda max} I_{solar(\lambda,\theta,\varphi)}\ \alpha_{solar(\lambda,\theta,\varphi)} d\lambda \,/\, \int_{\lambda min}^{\lambda max} I_{solar(\lambda,\theta,\varphi)}\ d\lambda \qquad (1)$$

where α is the solar absorption (%), λ is the wavelength (nm), λ_{min} and λ_{max} are 300 and 2500 nm, respectively. θ is the polar angle, and φ is the azimuthal angle. $I_{solar}(\lambda)$ is the AM1.5G solar spectral irradiance at λ, and $\alpha_{solar}(\lambda)$ is the light absorption (%) at λ. After the calculation, the solar absorption of TC composite aerogels was low to 20.2% (corresponding to the solar reflection of 79.8%). Meanwhile, the incorporation of BN nanosheets further decreases the solar absorption to 8.2% (corresponding to the solar reflection of 91.8%). Interestingly, the solar absorption of composite aerogel is lower than that of BN nanosheets, indicating an unexpected factor mainly due to the multi incidence-reflection modes (**Figure** 3a_3). In flat and dense structures, incident light successively goes through air, medium, and air, presenting two lines of reflection light. As presented by SEM photographs, there are a lot of air voids and cell walls that constitute the multilaminate interface. Therefore, multiple incidence-reflection will happen on the interfaces between the aerogel skeleton and air, further enhancing the solar reflection (Figure 3a_4)[20]. An outdoor experiment was performed to record the surface temperature of composite aerogel under solar illumination. The environment humidity is 53% and the solar intensity is ~0.9 kW/m^2 (Hefei, China). As presented in **Figures** 3a_1 and 3a_2, it is found that TC aerogel without BN nanosheets has an obvious solar absorption in 300-700 nm. Meanwhile, in **Figure** 2e, the surface temperature of TC aerogel is higher than that of TC/BN aerogel, at simulated sunlight of 1.0 kW/m^2. Therefore, it is anticipated that the radiative cooling effect of TC aerogel is lower than that of TC/BN aerogel. In recent reports, the radiative cooling effect of cellulose has been widely confirmed[25-27]. Based on such reasons, the radiative cooling effect of composite aerogel is compared with cellulose paper, when carrying out an outdoor experiment. It was found that the surface temperature of the paper crane prepared by cellulose is close to 41.6 ºC. In contrast, a lower surface temperature is presented in TC/BN composite

aerogel, near 39.9 °C (**Figures** 3b$_1$ and 3b$_2$). The temperature difference between TC/BN and cellulose may be due to the radiative cooling effect, relating closely to the reflectivity in the solar spectrum and IR emissivity in the atmospheric window. Therefore, the IR emissivity of TC/BN composite aerogel within the atmospheric window was further studied (**Figure** 3b$_3$). The overall IR emissivity in the atmospheric window is defined and calculated by equation (2)[24]:

$$\varepsilon(\lambda,\theta,\varphi) = \int_{\lambda\min}^{\lambda\max} I(\lambda,\theta,\varphi)\,\varepsilon(\lambda,\theta,\varphi)d\lambda \,/\, \int_{\lambda\min}^{\lambda\max} I(\lambda,\theta,\varphi)d\lambda \qquad (2)$$

where ε is the IR emissivity (%), λ is the wavelength (μm), λ_{min} and λ_{max} are 5 μm and 17 μm, respectively. θ is the polar angle, and φ is the azimuthal angle. I(λ) means the spectral intensity emitted by the blackbody at λ. It is found that the overall IR emissivity of TC/BN composite aerogel in the atmospheric window is up to 84.3%, may be due to the vibration of chemical bonds in BN and sodium alginate [21, 28]. As presented in the FTIR spectrum, BN nanosheets present a strong characteristic absorption peak near 12.44 μm, corresponding to the FTIR wavenumber of 803.86 cm^{-1} generated from the out-of-plane bending vibration of B-N-B bond (**Figure** 3b$_4$). Two broad characteristic absorption peaks centered in 13.8 μm (724.6 cm^{-1}) and 12.5 μm (800 cm^{-1}) in the FTIR spectrum of sodium alginate are assigned to the vibration of uronic acid. In addition, the broad peak ranging from 8.6 μm to 10 μm is assigned to the stretching vibration of C-O-C groups in sodium alginate. These characteristic peaks in BN nanosheets and sodium alginate are coincident with the atmospheric transparency window. For further investigating the radiative cooling effect, a continuous test of more than 8h was also performed under humidity of 46-53% and solar intensity of 300-1000 W/m^2. The schematic for the test configuration is shown in **Figure** S10. With the solar reflection of aluminum foil and thermal insulation of PS foam, thermal transmission and thermal convection are significantly suppressed. In addition, highly IR-transparent polyethylene (PE) film covered the surfaces of TC and TC/BN composite aerogel. The clear weather recorded by digital photos is attributed to the radiation of heat to outer space (**Figure** 3c$_1$). The highest temperature is

presented in TC aerogel, corresponding to the absorption of partial solar energy shown in **Figure** 3a_2. Compared to environment temperature, it is found that TC/BN composite aerogel can achieve an average temperature drop of ~5.62 °C (**Figure** 3c_2). The more effective cooling effect compared with the rare test presented in **Figures** 3b_1 and 3b_2 is attributed to the elimination of thermal transmission and thermal convection. Therefore, this sub-ambient temperature in TC/BN composite aerogel with the daytime radiative cooling effect can effectively decrease the energy consumption of buildings caused by air conditioning cooling.

The introduction of thermochromic microcapsules can impart the TC/BN composite aerogel with the ability of color change, under different environment temperatures. Taken from 0 ^{o}C to ~20 ^{o}C, the color of TC/BN composite aerogel gradually transfers to white from black in a short time (**Figure** 4a_1). In addition, the color change process of TC, BN, and TC/BN composite aerogels treated with liquid nitrogen was also recorded, providing a cold environment (**Figures** 4a_2 and S11). Before the treatment of liquid nitrogen, all samples present white appearances (at 0s). After being treated with liquid nitrogen, the environment temperature is rapidly decreased and the aliphatic alcohol is in a condensed state, thus repelling bisphenol A. As a result, bisphenol A interacts with 2-Anilino-6-dibutylamino-3-methylfluoran to suffer from an electron transfer process, thus constructing a conjugate structure. Therefore, the appearance of TC and TC/BN composite aerogels rapidly becomes black. It is found that BN composite aerogel without TC microcapsule demonstrates a white appearance all the time. The deep-black morphology in TC and TC/BN composite aerogels indicates a potential photo-thermal conversion in a cold environment, thus being employed in smart thermal regulation. The solar absorption of TC microcapsules and TC/BN aerogel under a cold environment is also studied by the UV-vis-Near IR spectrum. It is found that TC microcapsules and TC/BN aerogel demonstrate a high solar absorption in 300-650 nm, overlapping with the UV-vis range (**Figure** 4b). Compared to the solar absorptivity of up to 95% in 300-650 nm of TC microcapsules, the solar absorptivity of TC/BN composite aerogel is decreased to 87%, attributed to the multiple

aerogel-air interfaces which promote the reflection effect. In addition, the solar absorption of TC microcapsules and TC/BN aerogel ranging from 650 nm to 1100 nm is significantly reduced, indicating the photo-thermal conversion effect of TC microcapsules and TC/BN aerogel depends on the solar absorption in UV-vis waveband, rather near IR range.

The photo-thermal conversion effect of TC/BN composite aerogels under an environment temperature of -8.8 ^{o}C is further investigated with a home-made device. Without any illumination at 0s, the TC/BN composite aerogel is deep-black, implying a strong photo-thermal conversion effect (**Figure** 4c). After being illuminated by simulated sunlight of 1.0 kW/m^2, the color in the surface of TC/BN composite aerogel gradually becomes gray-white within 50s. Based on the thermochromic mechanism, the gray-white color indicates a higher temperature compared to the melting point of mixed fatty alcohol. The IR thermal imagery of TC/BN composite aerogel also confirms that the temperature is increased by 28.3 ^{o}C, to ~16.9 ^{o}C from -11.4 ^{o}C (**Figures** 4d$_1$ and S12). Presented by the heating curve, the surface temperature rapidly achieves the equilibrium temperature in 50s (Figure S13). Without the addition of TC microcapsules, the photo-thermal conversion effect isn't presented in BN composite aerogel. The surface temperature of BN composite aerogel is slightly increased to ~8.3 ^{o}C, attributed to the heating effect of near IR light contained in simulated sunlight (**Figures** 4d$_2$ and S14). In addition, the smart photo-thermal conversion effect of TC/BN composite aerogel is also compared with previous literature reporting other photo materials in normal and cold environments. As presented in **Figure** 4e, it is found that the increased temperature (~21.2 ^{o}C) of TC/BN composite aerogel is lower than those of non-adjustive photo-thermal materials, under one sun and normal temperature[29-36]. These photo-thermal materials including graphene, CNT, MXene, carbon black, and so on, present significant temperature increases (from 30 to 95 ^{o}C). The temperature increase of TC/BN composite aerogel in a cold environment is also evaluated in previous reports[37-40] (**Figure** 4e). Even though the surface

temperature is not the highest, an acceptable photo-thermal conversion effect is still presented by the increased temperature (~28.3 ^{o}C).

The energy-saving efficiency of TC/BN composite aerogel applied onto the surface of buildings is calculated by EnergyPlus simulation, as presented in **Figure** 4f$_1$. Detailed parameters, including building model and material properties, are provided in the experimental section. For conforming to practical application, $CaCO_3$ is chosen as the control material. Referred to previous literature, the solar absorption and IR emissivity of $CaCO_3$ are set as 0.1 and 0.7[41, 42]. Alaska, Mohe, and Yakutsk are chosen as cold cities. Once the indoor temperature is lower than 20 ^{o}C, the heating system will be run. Meanwhile, the cooling system does not exist. It is found that the heating consumption of building model in Alaska, Mohe, and Yakutsk are up to 1305.72 GJ, 2160.08 GJ, and 2971.11 GJ (**Figure** 4f$_2$). With the cover of TC/BN composite aerogel with a thickness of 3.0 mm onto the outer wall of the building model, the corresponding energy consumption is decreased to 1261.04 GJ, 2101.22 GJ, and 2926.6 GJ, presenting reductions of 44.68 GJ, 58.86 GJ, and 44.51 GJ. Meanwhile, Cairo, Singapore, and New Delhi are selected as hot cities. Higher than 26 ^{o}C, the cooling system will be opened. Compared to high energy consumption (475.83 GJ, 742.38 GJ, and 756.48 GJ), the cover of TC/BN composite aerogel also reduces the cooling consumption to 465.72 GJ, 727.19 GJ, and 742.97 GJ (**Figure** 4f$_3$). Even though the decrease ratio (1.5~3.4%) in building energy consumption is not significant, the accumulated amount of energy saving in the tens of thousands of cities and buildings will be extremely tremendous. Meanwhile, the simulation results in hot and cold cities also strongly confirm the universality of TC/BN composite aerogel on a global scale.

The color change mechanism is attributed to the temperature-sensitive melt feature of fatty alcohol and the selective dissolution of bisphenol A (**Figure** 4g). At low temperatures, aliphatic alcohol will be in a solidification state. Fluorane and bisphenol A are not dissolved into fatty alcohol. Therefore, bisphenol A and fluorane will be blended and form a conjugated structure

to absorb and convert solar energy (**Figure** 4g_1). More than the melting point, fatty alcohol will be in a melting state and bisphenol A can be dissolved into molten fatty alcohol. However, fluorane is still not dissolved into melting fatty alcohol. As a result, bisphenol A and fluorane will be separated, thus presenting a colorless appearance (**Figure** 4g_2). The smart thermal regulation based on solar thermal conversion and the radiative cooling effect is further analyzed. Under the condition of thermal equilibrium, the gain net power of P_{net} can be referred to as Equation 3[24, 43, 44]:

$$P_{net}(T) = P_{solar} + P_{atm}(T_{amb}) + P_{conv+cond} - P_{rad}(T) \quad (3)$$

where P_{rad} represents the energy that the sample emits outward, P_{solar} is the radiation received from the sun, P_{atm} is the radiation from the atmosphere, T is the surface temperature, T_{amb} is the ambient temperature, and the material also performs nonradiative heat exchange with the environment through thermal conduction and convection ($P_{conv+cond}$). Obviously, with the change in environment temperature, the P_{solar} of TC/BN composite aerogel is changed correspondingly (**Figure** 4g_3). Meanwhile, the $P_{conv+cond}$ will be also influenced by the temperature difference between the environment and TC/BN composite aerogel. The $P_{conv+cond}$ will promote the temperature consistency of TC/BN composite aerogel with the environment, thus leading to a negative effect on temperature regulation. In a cold environment, TC/BN composite aerogel presents an effective solar thermal conversion, thus significantly harvesting solar energy. As a result, the P_{net} (T) will be increased substantially. In a hot environment, TC/BN composite aerogel will reflect solar energy. Meanwhile, the heat is radiated continuously to outer space with the transparent atmospheric window. Therefore, the P_{net} (T) will be decreased correspondingly. Obviously, in responding to the dynamic environment, the changing P_{net} (T) contributes to imparting stable temperature to the material surface.

3.3. Fireproof performance of bio-based composite aerogels

As reported by previous literature, BN nanosheets have extreme resistance to high temperatures [45]. Meanwhile, the stable layer structure of BN nanosheets can suppress the delivery of pyrolysis products and oxygen during combustion. Besides, the synergistic effect between sodium alginate and phytic acid is capable of promoting the formation of a protective layer[46]. Presented in **Figure** 5, the heat release behavior of composite aerogel is evaluated by the cone calorimeter test. Compared to most polymer materials, the heat release curve of TC aerogel is broad relatively, without a keen-edged shape (**Figure** $5a_1$) [47]. Meanwhile, the peak value of heat release rate (PHRR) and total heat release (THR) of TC aerogel are 164.6 kW/m^2 and 15.4 MJ/m^2, respectively (**Figures** $5a_1$ and $5a_2$). These results indicate a low fire hazard for TC aerogel, attributed to the intrinsic flame retardancy of SA and PA. The introduction of BN nanosheets further decreases the fire hazards of TC/BN composite aerogel, presenting PHRR of 48.4 kW/m^2 and THR of 6.4 MJ/m^2. The flat and broad heat release peak in TC/BN composite aerogel may be due to the formation of a dense char layer that suppresses the combustion reaction. The PHRR and THR of TC/BN composite aerogel are decreased by 70.6% and 58.4%, respectively, compared to those of TC composite aerogel. The significant decreases in heat release rate and total heat release confirm that the incorporated BN nanosheets are capable of improving the fire safety of TC/BN composite aerogel. With the micro-calorimeter (MCC) test, the fire hazards of composite aerogel are further investigated (**Figure** 5b). Three heat release peaks are presented for TC composite aerogel. The first weak heat release peak is presented near 250 ^oC, due to the thermal degradation of fatty alcohol or hydroxyl and carboxyl groups[48]. The second and highest heat release peak is attributed to the combustion of pyrolysis products from the main chain of sodium alginate, presenting the peak value of heat release rate (PHRR) of up to 209.7 W/g. The oxidation of char residue causes the third heat release peak. The introduction of BN nanosheets effectively suppresses the heat release of composite aerogels. The PHRR value of TC/BN composite aerogel is decreased to 133.1 W/g,

presenting reductions of 36.5%. Interestingly, incorporated BN nanosheets lead to the disappearance of the third peak in TC/BN composite aerogel. This result also confirms that the introduction of BN nanosheets can effectively suppress the further oxidation of char residue[49]. As a result, the protective char layer can be effectively reserved, thus isolating the fire and inflammable products.

A fireproof test is performed to investigate the fire safety of bio-based TC/BN composite aerogel. It is found that the TC composite aerogel will be ignited by fire at 15s (**Figure** 5c_1). The grown fire also ignites the above paper at 35s, remarked by red narrow. It is found that the addition of BN nanosheets significantly increases the fireproof performance (**Figure** 5c_2). Compared to TC composite aerogel, TC/BN nanosheets do not present a fierce combustion phenomenon. During the combustion process, the fire is gradually extinguished at 50s. Meanwhile, the above paper is not ignited, indicating a potential fireproof performance. These results indicate that the incorporation of BN nanosheets can enhance the fireproof performance of bio-based composite aerogel, which may be attributed to the synergetic mechanism among sodium alginate, sodium phytic, and BN nanosheets[50]. The combustion residue of TC/BN composite aerogel is further observed (**Figure** 5d). It is found that the char layer can be divided into three layers. The white outermost layer can be BN nanosheets, without char residue (**Figure** 5d_1)[51]. The middle layer shows a brownish appearance, maybe due to the composition of more BN nanosheets and less char. The transitional middle layer also indicates that different mechanisms together impart well-fireproof performance to TC/BN composite aerogel (**Figure** 5d_2). The black appearance is presented in the innermost layer, which also occupies the most residue (**Figure** 5d_3). Due to the preparation process of composite aerogel, this black char residue also contains BN nanosheets. However, even with white BN nanosheets, white appearance is hard to find, confirming the high carbonization degree of TC/BN composite aerogel after the combustion[52].

The TGA test is carried out to investigate the thermal stability of TC/BN composite aerogel (**Figures** 5e_1 and 5e_2). Lower than 230 ^oC, the mass loss of ~10wt% is mainly attributed to the carboxyl group of sodium alginate or fatty alcohol. The thermal degradation of hydroxyl and ether bond together leads to mass loss in 230-330 ^oC. It is found that, at more than 330 ^oC, the nitrogen and air atmospheres cause different thermal degradation behaviors, attributed to the pyrolysis of the main chain and char layer[53]. The char residue at 800 ^oC of TC aerogel is 20.1 wt% and 26.7 wt%, corresponding to air and nitrogen atmospheres. Accordingly, the introduction of BN nanosheets increases char residue to 60.5 wt% and 61.1 wt%. The practical addition amount of BN nanosheets is 35.7wt%. Meanwhile, the TGA curve in the nitrogen atmosphere indicates that BN nanosheets can maintain a stable weight under 800 ^oC (**Figure** S15). Therefore, the theoretical char residue in TC/BN composite aerogel should be 48.6wt% and 52.9wt%. The higher char residue in the experimental result indicates that the introduction of BN nanosheets effectively promotes the formation of protective char residue in the air atmosphere[54]. The gaseous pyrolysis products of TC and TC/BN composite aerogels are also studied by the TG-IR spectrum (**Figure** 5f). The 3D TG-IR spectra of TC and TC/BN composite aerogels are presented in **Figures** 5f_1 and S16. The characteristic peaks at 2820 cm^{-1}, 2360 cm^{-1}, 2180 cm^{-1}, and 1740 cm^{-1} are attributed to the production of hydrocarbons, CO_2, CO, carbonyl compounds[55]. Even with the addition of BN nanosheets, the main thermal pyrolysis products are nearly the same, as shown in the profile chart of 3D TG-IR spectra (**Figure** 5f_2). In fact, the high thermal stability also makes BN nanosheets not directly participate in the thermal pyrolysis process of TC/BN composite aerogel. After being divided by sample mass, the absorbance intensity of total pyrolysis products and hydrocarbons, CO_2, CO, and carbonyl compounds are directly employed to investigate the release amount of pyrolysis products (**Figures** 5f_3-f_7). It is found that the addition of BN nanosheets does not change the time corresponding to the characteristic peaks. This phenomenon also confirms that BN nanosheets does not directly participate in the thermal pyrolysis process of TC/BN composite aerogel. Besides, incorporated

BN nanosheets effectively reduce the peak intensity, indicating less pyrolysis products[56]. Based on the TGA and TG-IR results, it is demonstrated that the introduction of BN nanosheets effectively suppresses the thermal pyrolysis process of TC/BN composite aerogel, confirmed by more condensed char residue and less gaseous products. Based on the above analyses, a probable fireproof mechanism is put forward (**Figure** 5g). In the outermost layer, sodium alginate and phytic acid will be first burned thoroughly to produce residue of BN nanosheets[57]. The white shell in the char residue confirms this view. The produced BN-based shell then promotes the carbonization reaction between sodium alginate as a carbon source and sodium phytate as an acid source[58]. The brown transition layer and black core confirm the effect and participation of BN nanosheets in the formation of a protective char layer. Especially, the TGA and MCC results indicate that the introduction of BN nanosheets can suppress the degradation of a protective layer, with high thermal stability and layer structure.

4. Conclusion

Based on the design and integration of multiple functional components, a bio-inspired, sustainable, fire-safe composite aerogel towards smart thermal regulation was prepared by combining thermochromic microcapsule, BN nanosheets, sodium alginate, and sodium phytate. In addition to the large bandgap and high refractive index of BN nanosheets, multiple incidence-reflection modes caused by the air-aerogel interface further increase the solar reflection of composite aerogel to 91.8%. Under simulated sunlight of 1.0 kW/m^2, the surface temperature of composite aerogel is only increased to 49.8 ^{o}C. With IR emissivity of ~84.3%, TC/BN composite aerogel demonstrates an average temperature drop of ~5.62 °C compared with the environment. Meanwhile, based on the temperature-controlled switch between melting and solidification of aliphatic alcohol, the reversible formation of conjugated structure within thermochromic microcapsule is capable of converting solar energy into heat. The photo-thermal effect of composite aerogel in cold environments also promotes solar harvest and increases the

temperature of TC/BN composite aerogel by 28.3 ^{o}C under an environment of -8.8 ^{o}C. The high thermal stability and layer structure make BN nanosheets suppress the combustion process of TC/BN composite aerogel. Meanwhile, the pyrolysis products from sodium alginate and sodium phytic together construct a protective char layer, with the assistance of the barrier effect of BN nanosheets. As a result, this composite aerogel prepared isolates the delivery between fire and inflammable products. In conclusion, this multifunctional composite aerogel not only contributes to decreasing the huge energy consumption of buildings caused by indoor air condition, but also provides an available solution for the disposal of fire hazards of thermal management materials.

Acknowledgments

The authors acknowledge financial support from the National Key Research and Development Program of China (2022YFC3003100), the National Natural Science Foundation of China (22205228), the Fellowship of China Postdoctoral Science Foundation (2021M703054 and 2022T150613), Anhui Provincial Natural Science Foundation (2308085ME147). The preparation and technology of thermochromic microcapsules are conducted by Thousand-color Co., Ltd, Shenzhen. We would like to thank Dr. Hong Ye and Dr. Qing Ni from the School of Engineering Science, University of Science and Technology of China for their assistance in mid infrared spectroscopy analysis. Thanks to Dr. Jun Fang from the State Key Laboratory of Fire Science, University of Science and Technology of China for his help in instrument construction.

References:

[1] I. Staffell, S. Pfenninger, N.J.N.E. Johnson, A global model of hourly space heating and cooling demand at multiple spatial scales, Nat. Energy, (2023) 1-17.

[2] S. Zeng, S. Pian, M. Su, Z. Wang, M. Wu, X. Liu, M. Chen, Y. Xiang, J. Wu, M. Zhang, Q. Cen, Y. Tang, X. Zhou, Z. Huang, R. Wang, A. Tunuhe, X. Sun, Z. Xia, M. Tian, M. Chen, X.

Ma, L. Yang, J. Zhou, H. Zhou, Q. Yang, X. Li, Y. Ma, G. Tao, Hierarchical-morphology metafabric for scalable passive daytime radiative cooling, Science, 373 (2021) 692.
[3] H. Zhao, Q. Sun, J. Zhou, X. Deng, J. Cui, Switchable Cavitation in Silicone Coatings for Energy-Saving Cooling and Heating, Adv. Mater., 32 (2020) 2000870.
[4] W.L. Fu, L.L. Tan, P.P. Wang, Chiral Inorganic Nanomaterials for Photo(electro)catalytic Conversion, Acs Nano, (2023) 16326.
[5] X. Zhang, W. Yang, Z. Shao, Y. Li, Y. Su, Q. Zhang, C. Hou, H. Wang, A Moisture-Wicking Passive Radiative Cooling Hierarchical Metafabric, ACS Nano, 16 (2022) 2188-2197.
[6] Y.Q. Chen, J.J. Hao, J. Xu, Z.S. Hu, H.F. Bao, H.L. Xu, Pickering Emulsion Templated 3D Cylindrical Open Porous Aerogel for Highly Efficient Solar Steam Generation, Small, (2023) 2303908.
[7] P. Wu, X. Wu, Y.D. Wang, H.L. Xu, G. Owens, A biomimetic interfacial solar evaporator for heavy metal soil remediation, Chem. Eng. J., 435 (2022) 134793.
[8] K. Lin, S. Chen, Y. Zeng, T.C. Ho, Y. Zhu, X. Wang, F. Liu, B. Huang, C.Y.-H. Chao, Z.J.S. Wang, Hierarchically structured passive radiative cooling ceramic with high solar reflectivity, Science 382 (2023) 691-697.
[9] X. Zhao, T. Li, H. Xie, H. Liu, L. Wang, Y. Qu, S.C. Li, S. Liu, A.H. Brozena, Z.J.S. Yu, A solution-processed radiative cooling glass, Science 382 (2023) 684-691.
[10] S. Zeng, S. Pian, M. Su, Z. Wang, M. Wu, X. Liu, M. Chen, Y. Xiang, J. Wu, M. Zhang, Q. Cen, Y. Tang, X. Zhou, Z. Huang, R. Wang, A. Tunuhe, X. Sun, Z. Xia, M. Tian, M. Chen, X. Ma, L. Yang, J. Zhou, H. Zhou, Q. Yang, X. Li, Y. Ma, G. Tao, Hierarchical-morphology metafabric for scalable passive daytime radiative cooling, Science, 373 (2021) 692-696.
[11] C.X. Sui, J.K. Pu, T.H. Chen, J.W. Liang, Y.T. Lai, Y.F. Rao, R.H. Wu, Y. Han, K.Y. Wang, X.Q. Li, V. Viswanathan, P.C. Hsu, Dynamic electrochromism for all-season radiative thermoregulation, Nat. Sustain., 6 (2023) 428-437.
[12] X. Li, B. Sun, C. Sui, A. Nandi, H. Fang, Y. Peng, G. Tan, P.C. Hsu, Integration of daytime radiative cooling and solar heating for year-round energy saving in buildings, Nat. Commun., 11 (2020) 6101.
[13] M. Zimova, K. Hacklaender, J.M. Good, J. Melo-Ferreira, P.C. Alves, L.S. Mills, Function and underlying mechanisms of seasonal colour moulting in mammals and birds: what keeps them changing in a warming world?, Biol. Rev., 93 (2018) 1478-1498.
[14] S. Shen, L. Feng, S. Qi, J. Cao, Y. Ge, L. Wu, S. Wang, Reversible Thermochromic Nanoparticles Composed of a Eutectic Mixture for Temperature-Controlled Photothermal Therapy, Nano Lett., 20 (2020) 2137-2143.

[15] X. Geng, W. Li, Y. Wang, J. Lu, J. Wang, N. Wang, J. Li, X. Zhang, Reversible thermochromic microencapsulated phase change materials for thermal energy storage application in thermal protective clothing, Appl. Energy, 217 (2018) 281-294.
[16] D. Lee, B. Lee, K.H. Park, H.J. Ryu, S. Jeon, S.H. Hong, Scalable exfoliation process for highly soluble boron nitride nanoplatelets by hydroxide-assisted ball milling, Nano Lett., 15 (2015) 1238-1244.
[17] M. Li, M. Wang, N. Zhao, H. Bai, Scalable Fabrication of High-Performance Bulk Nacre-Mimetic Materials on a Nanogrooved Surface, Acs Nano, 16 (2022) 14737-14744.
[18] R. Li, S. Tian, Y. Tian, J. Wang, S. Xu, K. Yang, J. Yang, L. Zhang, An Extreme-Environment-Resistant Self-Healing Anti-Icing Coating, Small, (2022) 2206075.
[19] J.Y. Do, N. Son, J. Shin, R.K. Chava, S.W. Joo, M. Kang, n-Eicosane-Fe_3O_4@SiO_2@Cu microcapsule phase change material and its improved thermal conductivity and heat transfer performance, Mater. Design, 198 (2021) 109357.
[20] J. Yang, K.-Y. Chan, H. Venkatesan, E. Kim, M.H. Adegun, J.-H. Lee, X. Shen, J.-K. Kim, Superinsulating BNNS/PVA Composite Aerogels with High Solar Reflectance for Energy-Efficient Buildings, Nano-Micro Lett., 14 (2022).
[21] G. Chen, Y. Wang, Y. Zou, H. Wang, J. Qiu, J. Cao, S. Wang, D. Jia, Y. Zhou, Hexagonal boron nitride and alumina dual-layer coating for space solar thermal shielding, Chem. Eng. J., 421 (2021) 127802.
[22] Y.W. Li, T.Q. Huang, M. Chen, L.M. Wu, Simultaneous exfoliation and functionalization of large-sized boron nitride nanosheets for enhanced thermal conductivity of polymer composite film, Chem. Eng. J., 442 (2022) 136237.
[23] J.J. Li, Y.N. Chen, F.D. Zhang, Y. Lyu, X.N. Li, K. Li, J.Z. Li, Spider silk-inspired high-performance soybean meal-based adhesive reinforced by greenly produced chitosan-functionalized boron nitride nanosheets, Chem. Eng. J., 438 (2022) 135442.
[24] T. Yeamsuksawat, Y. Morishita, J. Shirahama, Y.T. Huang, T. Kasuga, M. Nogi, H. Koga, Semicarbonized Subwavelength-Nanopore-Structured Nanocellulose Paper for Applications in Solar Thermal Heating, Chem. Mater., 34 (2022) 7379.
[25] J. Jaramillo-Fernandez, H. Yang, L. Schertel, G.L. Whitworth, P.D. Garcia, S. Vignolini, C.M. Sotomayor-Torres, Highly-Scattering Cellulose-Based Films for Radiative Cooling, Adv. Sci., 9 (2022) e2104758.
[26] Y. Zhang, W. Zhu, C. Zhang, J. Peoples, X. Li, A.L. Felicelli, X. Shan, D.M. Warsinger, T. Borca-Tasciuc, X. Ruan, T. Li, Atmospheric Water Harvesting by Large-Scale Radiative Cooling Cellulose-Based Fabric, Nano Lett., 22 (2022) 2618.

[27] Y. Chen, B. Dang, J. Fu, C. Wang, C. Li, Q. Sun, H. Li, Cellulose-Based Hybrid Structural Material for Radiative Cooling, Nano Lett., 21 (2021) 397-404.
[28] A. Felicelli, I. Katsamba, F. Barrios, Y. Zhang, Z. Guo, J. Peoples, G. Chiu, X. Ruan, Thin layer lightweight and ultrawhite hexagonal boron nitride nanoporous paints for daytime radiative cooling, Cell Rep. Phys. Sci., 3 (2022) 10.
[29] H. Ren, M. Tang, B. Guan, K. Wang, J. Yang, F. Wang, M. Wang, J. Shan, Z. Chen, D. Wei, H. Peng, Z. Liu, Hierarchical Graphene Foam for Efficient Omnidirectional Solar-Thermal Energy Conversion, Adv. Mater., 29 (2017) 1702590.
[30] P. Cao, L. Zhao, J. Zhang, L. Zhang, P. Yuan, Y. Zhang, Q. Li, Gradient Heating Effect Modulated by Hydrophobic/Hydrophilic Carbon Nanotube Network Structures for Ultrafast Solar Steam Generation, Acs Appl. Mater. Inter., 13 (2021) 19109.
[31] X. Zhao, X.-J. Zha, L.-S. Tang, J.-H. Pu, K. Ke, R.-Y. Bao, Z.-y. Liu, M.-B. Yang, W. Yang, Self-assembled core-shell polydopamine@MXene with synergistic solar absorption capability for highly efficient solar-to-vapor generation, Nano Res., 13 (2020) 255-264.
[32] L. Sun, J. Liu, Y. Zhao, J. Xu, Y. Li, Highly efficient solar steam generation via mass-produced carbon nanosheet frameworks, Carbon, 145 (2019) 352-358.
[33] H. Zhong, Z. Zhu, J. Lin, C.F. Cheung, V.L. Lu, F. Yan, C.-Y. Chan, G. Li, Reusable and Recyclable Graphene Masks with Outstanding Superhydrophobic and Photothermal Performances, Acs Nano, 14 (2020) 6213.
[34] Y. Li, X. Jin, Y. Zheng, W. Li, F. Zheng, W. Wang, T. Lin, Z. Zhu, Tunable Water Delivery in Carbon-Coated Fabrics for High-Efficiency Solar Vapor Generation, Acs Appl. Mater. Inter., 11 (2019) 46938.
[35] C. Zhang, X. Peng, N. Feng, L. Yan, Q. Liu, D. Zhang, J. Gu, W. Wang, T. Chen, Converting Pomelo Peel into Eco-friendly and Low-Consumption Photothermic Biomass Sponge toward Multifunctioal Solar-to-Heat Conversion, Acs Sustain. Chem. Eng., 8 (2020) 5328-5337.
[36] Z. Guo, W. Zhou, N. Arshad, Z. Zhang, D. Yan, M.S. Irshad, L. Yu, X. Wang, Excellent energy capture of hierarchical MoS_2 nanosheets coupled with MXene for efficient solar evaporators and thermal packs, Carbon, 186 (2022) 19-27.
[37] C. Chen, Z. Tian, X. Luo, G. Jiang, X. Hu, L. Wang, R. Peng, H. Zhang, M. Zhong, Cauliflower-like micro-nano structured superhydrophobic surfaces for durable anti-icing and photothermal de-icing, Chem. Eng. J., 450 (2022) 137936.
[38] Z. Zhao, H. Chen, Y. Zhu, X. Liu, Z. Wang, J. Chen, A robust superhydrophobic anti-icing/de-icing composite coating with electrothermal and auxiliary photothermal performances,

643 Compos. Sci. Technol., 227 (2022) 109578.
644 [39] G. Jiang, Z. Liu, J. Hu, Superhydrophobic and Photothermal PVDF/CNTs Durable
645 Composite Coatings for Passive Anti-Icing/Active De-Icing, Adv. Mater. Interf., 9 (2022)
646 2101704.
647 [40] B. Yu, Z. Sun, Y. Liu, Z. Zhang, Y. Wu, F. Zhou, Improving Anti-Icing and De-Icing
648 Performances via Thermal-Regulation with Macroporous Xerogel, Acs Appl. Mater. Inter., 13
649 (2021) 37609-37616.
650 [41] Y. Da, J. Zhou, Microscopic mechanisms of Mn-doped $CaCO_3$ heat carrier with enhanced
651 optical absorption and accelerated decomposition kinetics for directly storing solar energy, Sol.
652 Energ. Mat. Sol. C., 250 (2023) 112103.
653 [42] H. Lim, D. Chae, S. Son, J. Ha, H. Lee, $CaCO_3$ micro particle-based radiative cooling
654 device without metal reflector for entire day, Mater. Today Commun., 32 (2022) 103990.
655 [43] J. Wang, D.S. Yuan, P.Y. Hu, Y.J. Wang, J. Wang, Q.W. Li, Optical Design of Silica
656 Aerogels for On-Demand Thermal Management, Adv. Funct. Mater., (2023) 2300441.
657 [44] B. Ma, Y. Cheng, P. Hu, D. Fang, J. Wang, Passive Daytime Radiative Cooling of Silica
658 Aerogels, Nanomaterials (Basel), 13 (2023) 467.
659 [45] G. Han, X. Zhao, Y. Feng, J. Ma, K. Zhou, Y. Shi, C. Liu, X. Xie, Highly flame-retardant
660 epoxy-based thermal conductive composites with functionalized boron nitride nanosheets
661 exfoliated by one-step ball milling, Chem. Eng. J., 407 (2021) 127099.
662 [46] S. Han, F. Yang, Q. Li, G. Sui, X. Su, J. Dai, J.J.P.D. Ma, Stability, Tackling smoke toxicity
663 and fire hazards of thermoplastic polyurethane by mechanochemical combination of Cu_2O
664 nanoparticles and zirconium phosphate nanosheets, Polym. Degrad. Stabil., 212 (2023) 110350.
665 [47] S.Q. Huo, P.A. Song, B. Yu, S.Y. Ran, V.S. Chevali, L. Liu, Z.P. Fang, H. Wang,
666 Phosphorus-containing flame retardant epoxy thermosets: Recent advances and future
667 perspectives, Prog. Polym. Sci., 114 (2021) 101366.
668 [48] L. Sun, H. Wang, W. Li, J. Zhang, Z. Zhang, Z. Lu, P. Zhu, C. Dong, Preparation,
669 characterization and testing of flame retardant cotton cellulose material: flame retardancy,
670 thermal stability and flame-retardant mechanism, Cellulose, 28 (2021) 3789-3805.
671 [49] X. Li, Y. Feng, C. Chen, Y. Ye, H. Zeng, H. Qu, J. Liu, X. Zhou, S. Long, X. Xie, Highly
672 thermally conductive flame retardant epoxy nanocomposites with multifunctional ionic liquid
673 flame retardant-functionalized boron nitride nanosheets, J. Mater. Chem. A, 6 (2018) 20500-
674 20512.
675 [50] S. Han, F. Yang, Q. Meng, J. Li, G. Sui, X. Su, H.-C. Kuan, C.H. Wang, J.J.P.i.O.C. Ma,
676 Using renewable phosphate to decorate graphene nanoplatelets for flame-retarding,

677 mechanically resilient epoxy nanocomposites, Prog. Org. Coat. 182 (2023) 107658.
678 [51] Y. Xu, X. Zhang, Z. Liu, X. Zhang, J. Luo, J. Li, S.Q. Shi, J. Li, Q. Gao, Constructing SiO_2
679 nanohybrid to develop a strong soy protein adhesive with excellent flame-retardant and coating
680 ability, Chem. Eng. J., 446 (2022) 137065.
681 [52] S. Araby, J. Li, G. Shi, Z. Ma, J.J.C.P.A.A.S. Ma, Manufacturing, Graphene for flame-
682 retarding elastomeric composite foams having strong interface, Compos. Part A: Appl. S 101
683 (2017) 254-264.
684 [53] P. Halder, S. Kundu, S. Patel, R. Parthasarathy, B. Pramanik, J. Paz-Ferreiro, K. Shah,
685 TGA-FTIR study on the slow pyrolysis of lignin and cellulose-rich fractions derived from
686 imidazolium-based ionic liquid pre-treatment of sugarcane straw, Energ. Convers. Manage.,
687 200 (2019) 112067.
688 [54] S. Araby, C.-H. Wang, H. Wu, Q. Meng, H.-C. Kuan, N.K. Kim, A. Mouritz, J.J.C.P.A.A.S.
689 Ma, Manufacturing, Development of flame-retarding elastomeric composites with high
690 mechanical performance, Compos. Part A: Appl. S. 109 (2018) 257-266.
691 [55] Z.H. Wang, B.W. Liu, F.R. Zeng, X.C. Lin, J.Y. Zhang, X.L. Wang, Y.Z. Wang, H.B. Zhao,
692 Fully recyclable multifunctional adhesive with high durability, transparency, flame retardancy,
693 and harsh-environment resistance, Sci. Adv., 8 (2022) 8527.
694 [56] H. Wu, S. Araby, J. Xu, H.-C. Kuan, C.-H. Wang, A. Mouritz, Y. Zhuge, R.J.-T. Lin, T.
695 Zong, J.J.C.P.A.A.S. Ma, Manufacturing, Filling natural microtubules with triphenyl phosphate
696 for flame-retarding polymer composites, Compos. Part A: Appl. S. 115 (2018) 247-254.
697 [57] M. Weinmann, J. Schuhmacher, H. Kummer, S. Prinz, J.Q. Peng, H.J. Seifert, M. Christ,
698 K. Muller, J. Bill, F. Aldinger, Synthesis and thermal behavior of novel Si-B-C-N ceramic
699 precursors, Chem. Mater., 12 (2000) 623-632.
700 [58] W. Zhu, M. Yang, H. Huang, Z. Dai, B. Cheng, S. Hao, A phytic acid-based chelating
701 coordination embedding structure of phosphorus-boron-nitride synergistic flame retardant to
702 enhance durability and flame retardancy of cotton, Cellulose, 27 (2020) 4817-4829.
703
704

Figure caption

Figure 1 Schematic diagram of multifunctional aerogels. Ideal solar reflection (a) and absorption (b) curves in hot and cold environments; (c) The molt phenomenon of polar hare in summer and winter (with permission.[13] Copyright 2018, Wiley) and the molecular formula of melatonin; (d) The thermochromic mechanism between fluorane and bisphenol A: fluorane can reversibly react with bisphenol A to produce a conjugated structure which can absorb solar energy; (e) The preparation schematic diagram of thermochromic microcapsules based on the microencapsulation technology with the interfacial polymerization: bisphenol A, 2-anilino-6-dibutylamino-3-methylfluoran, and aliphatic alcohol are encapsulated by melamine resin; (f) The preparation schematic of TC/BN composite aerogels with the directional freeze-drying method: sodium alginate and sodium phytic are used as aerogel skeleton, while BN nanosheets and TC microcapsule are added as functional fillers; (g) The smart thermal regulation modes based on the solar thermal conversion under cold weather and radiative cooling under hot weather.

Figure 2 Morphologies and optical properties of thermochromic microcapsules, BN nanosheets, and composite aerogel. (a) Color change of thermochromic microcapsules from black in cold temperature to gray-white in normal temperature; (b_1) SEM photograph of thermochromic microcapsules showing a spherical morphology; (b_2) DSC curve of thermochromic microcapsules; (c_1) Digital photo and (c_2) 3D schematic of TC/BN composite aerogel which has a pure white color; SEM photograph of top view (d_1) and cross-section (d_2-d_4) of TC/BN composite aerogel; (d_5) SEM EDS Mapping spectra of TC/BN composite aerogel; (e) IR thermal imaging of TC/BN and TC composite aerogels under simulated one sun.

Figure 3 Optical properties and outdoor radiative cooling experiment. (a_1) Solar absorption spectra of BN nanosheets, TC microcapsules, and sodium alginate; (a_2) Solar absorption spectra of TC and TC/BN composite aerogels; (a_3) Solar absorption spectra of BN nanosheets, TC, and TC/BN composite aerogels; (a_4) Schematic for the multi reflection in air-aerogel interface; IR

thermal imaging of paper crane (b_1) and TC/BN composite aerogel (b_2) in a field test (Hefei, China), presenting surface temperature of 41.6 ^oC and 39.9 ^oC, respectively; (b_3) IR emissivity spectrum of TC/BN composite aerogel; (b_4) FTIR spectra of BN and sodium alginate; (c_1) Test environment presented by digital photo; (c_2) Temperature curves of air, TC, and TC/BN composite aerogels with an LDPE cover.

Figure 4 The thermal regulation performance of composite aerogels. Color change of TC/BN composite aerogel taken from 0 ^oC environment (a_1) and treated by liquid nitrogen (a_2); (b) Solar absorption spectra of TC and TC/BN aerogel under cold environments; (c) Color change process versus time of TC/BN composite aerogel under a cold environment, with simulated sunlight of 1.0 kW/m^2; IR thermal imaging of TC/BN composite aerogel (d_1) and BN composite aerogel (d_2) under simulated radiation of 1.0 kW/m^2; (e) The comparison results of surface temperature of TC/BN composite aergel with previous research works, under cold and normal enviroments with 1.0 sun; (f_1) Building Modeling of the EnergyPlus simulation to calculate the energy-saving efficiency; Energy-saving efficiency for cold (f_2) and hot (f_3) cities; Mechanism diagram of change color of composite aerogels under cold (g_1) and hot environments (g_2); (g_3) Mechanism diagram for the temperature regulation behaviors of TC/BN composite aerogels.

Figure 5 Fire safety performance, thermal pyrolysis process, and fireproof mechanism of TC/BN composite aerogel. (a_1) HRR and THR (a_2) curves of TC and TC/BN composite aerogels with cone calorimeter test; (b) HRR curves of TC and TC/BN composite aerogels with micro-calorimeter test; The fireproof test of TC (c_1) and TC/BN composite aerogels (c_2); Digital photo of char residue of TC/BN composite aerogel, presenting different morphologies in outer (d_1), middle (d_2), and inner parts (d_3); TGA curves of TC, BN, TC/BN composite aerogels under nitrogen (e_1) and air (e_2) atmospheres; (f_1) 3D TG-IR spectra of TC composite aerogel; (f_2) Profile chart of 3D TG-IR spectra of the pyrolysis gaseous products emitted from TC and TC/BN composite aerogels at the maximum degradation rate; Absorbance of pyrolysis products

for TC and TC/BN composite aerogels vs time (f_3-f_7); (g) The schematic diagram of fireproof mechanism of TC/BN composite aerogel.

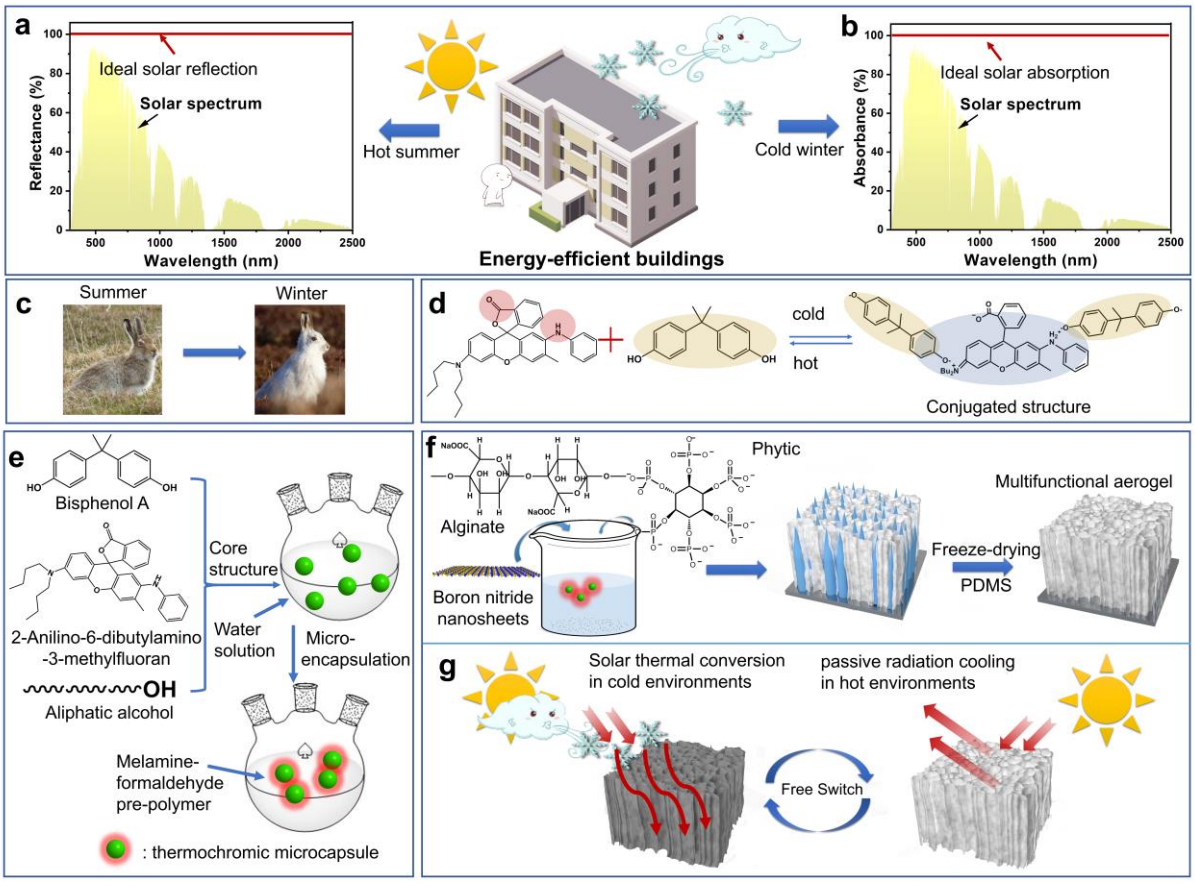
a
Ideal solar reflection
Solar spectrum
Reflectance (%)
Wavelength (nm)
Hot summer
Energy-efficient buildings
Cold winter
b
Ideal solar absorption
Solar spectrum
Absorbance (%)
Wavelength (nm)
c
Summer
Winter
d
cold
hot
Conjugated structure
e
Bisphenol A
2-Anilino-6-dibutylamino
-3-methylfluoran
Aliphatic alcohol
Core
structure
Water
solution
Micro-
encapsulation
Melamine-
formaldehyde
pre-polymer
: thermochromic microcapsule
f
Phytic
Alginate
Boron nitride
nanosheets
Multifunctional aerogel
Freeze-drying
PDMS
g
Solar thermal conversion
in cold environments
passive radiation cooling
in hot environments
Free Switch

Figure 1

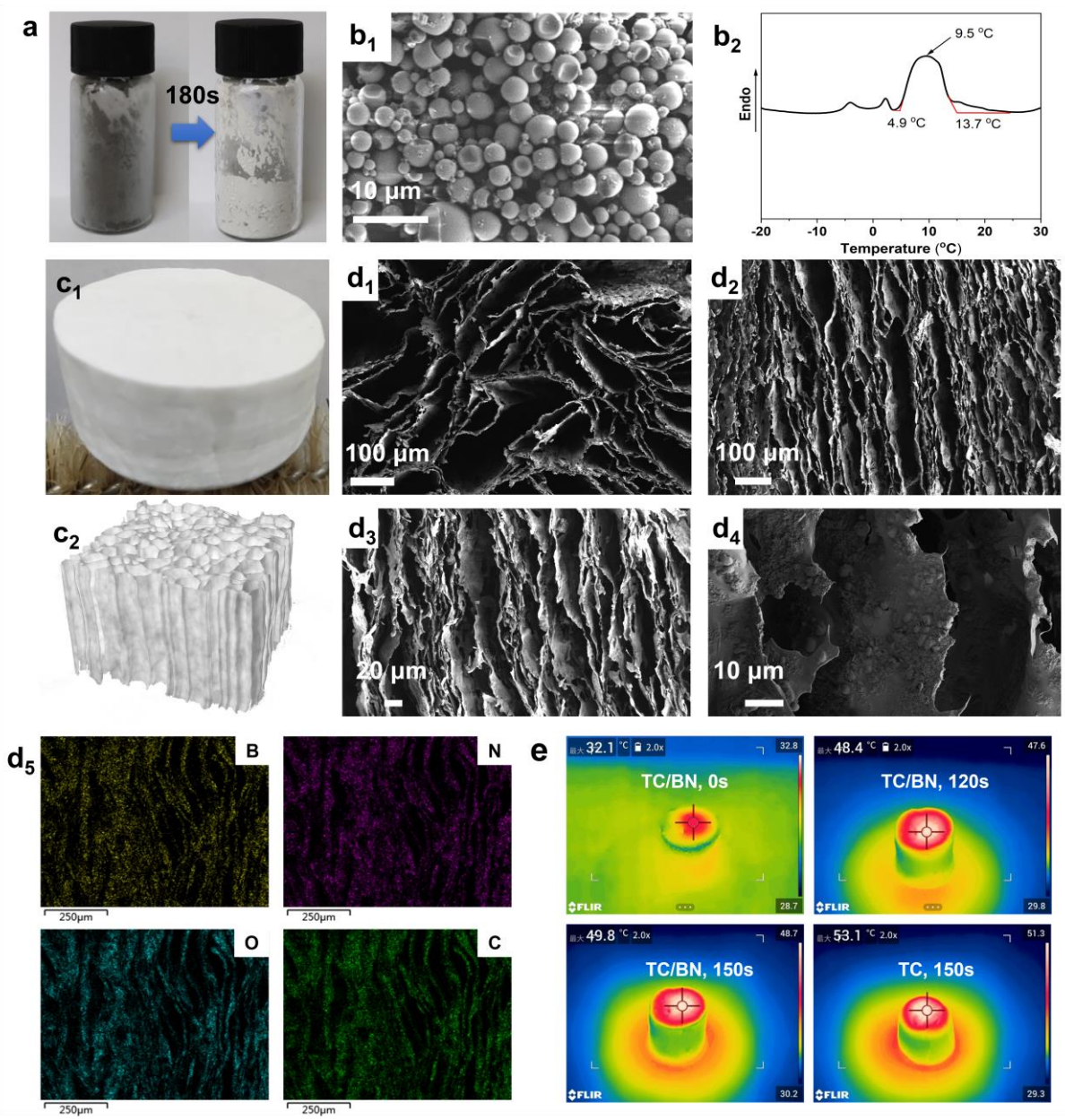
a
180s
b1
10 μm
b2
9.5 °C
Endo
4.9 °C
13.7 °C
-20
-10
0
10
20
30
Temperature (°C)
c1
c2
d1
100 μm
d2
100 μm
d3
20 μm
d4
10 μm
d5
B
N
O
C
250μm
e
32.1 °C
TC/BN, 0s
48.4 °C
TC/BN, 120s
49.8 °C
TC/BN, 150s
53.1 °C
TC, 150s
FLIR

Figure 2

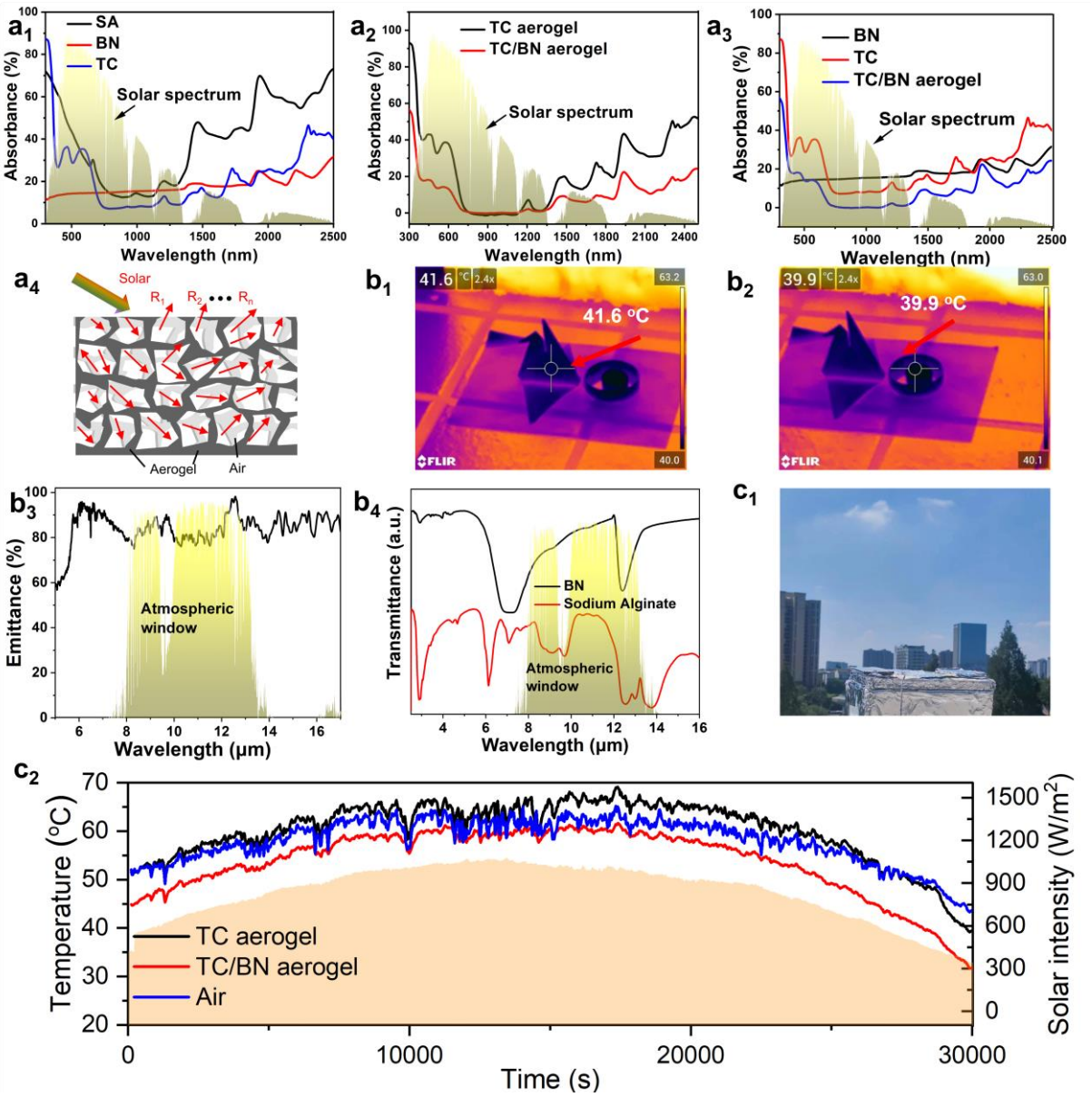

763

764 **Figure 3**

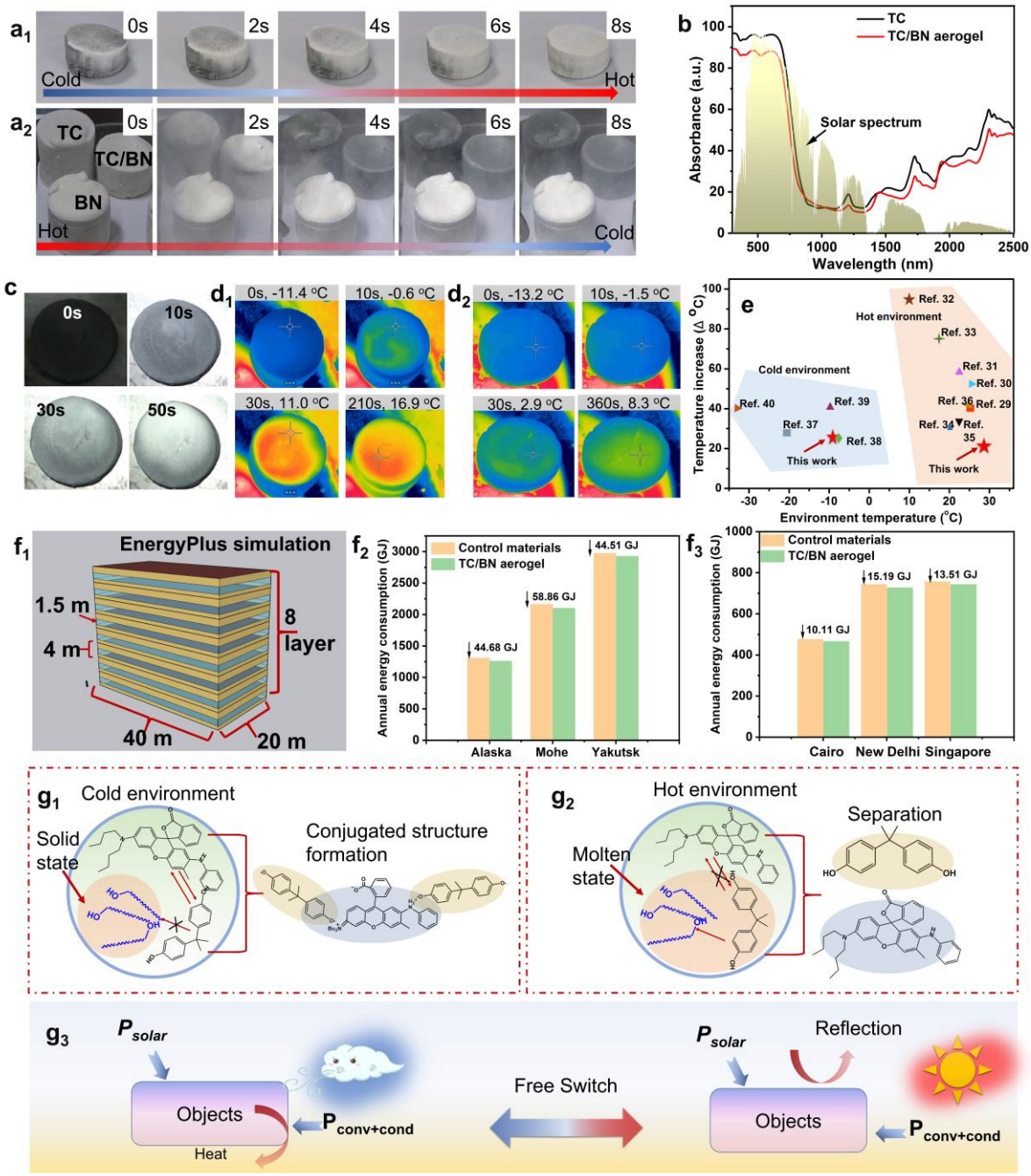

765

766 **Figure 4**

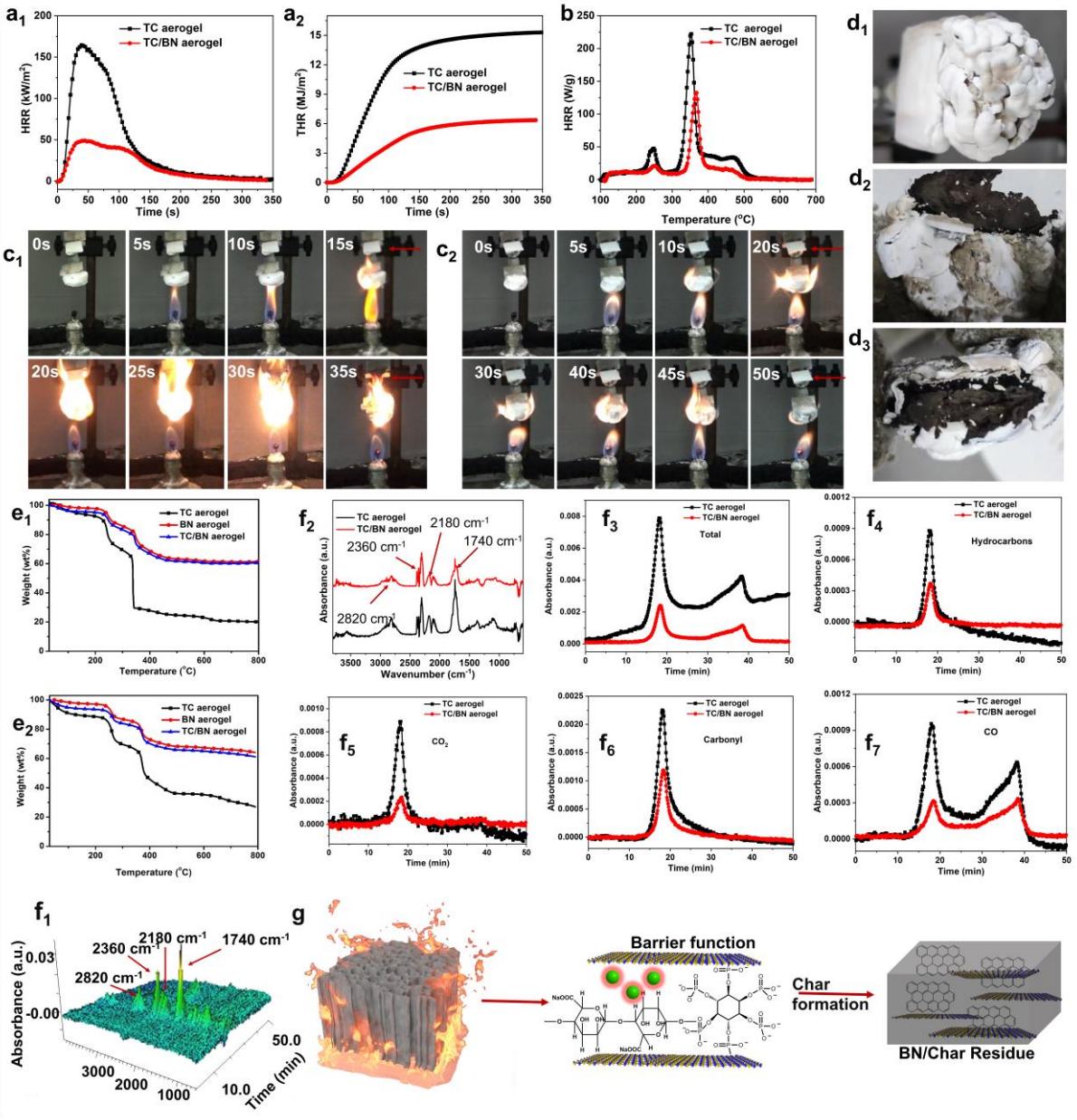
a1
TC aerogel
TC/BN aerogel
HRR (kW/m²)
Time (s)
a2
THR (MJ/m²)
b
HRR (W/g)
Temperature (°C)
d1
d2
d3
c1
0s
5s
10s
15s
20s
25s
30s
35s
c2
0s
5s
10s
20s
30s
40s
45s
50s
e1
BN aerogel
Weight (wt%)
Temperature (°C)
f2
2180 cm-1
2360 cm-1
1740 cm-1
2820 cm-1
Absorbance (a.u.)
Wavenumber (cm-1)
f3
Total
Time (min)
f4
Hydrocarbons
e2
f5
CO2
f6
Carbonyl
f7
CO
f1
g
Barrier function
Char formation
BN/Char Residue

Figure 5